A New Class of Roche Lobe–filling Hot Subdwarf Binaries

Thomas Kupfer[1] , Evan B. Bauer[1] , Kevin B. Burdge[2] , Jan van Roestel[2] , Eric C. Bellm[3] , Jim Fuller[2] , JJ Hermes[4] ,
Thomas R. Marsh[5] , Lars Bildsten[1,6], Shrinivas R. Kulkarni[2] , E. S. Phinney[7] , Thomas A. Prince[2] , Paula Szkody[8] ,
Yuhan Yao[2] , Andreas Irrgang[9] , Ulrich Heber[9] , David Schneider[9], Vik S. Dhillon[10,11] , Gabriel Murawski[12] ,
Andrew J. Drake[2], Dmitry A. Duev[2] , Michael Feeney[13], Matthew J. Graham[2] , Russ R. Laher[14] , S. P. Littlefair[10] ,
A. A. Mahabal[2,15] , Frank J. Masci[14] , Michael Porter[13], Dan Reiley[13], Hector Rodriguez[13], Ben Rusholme[14] ,
David L. Shupe[14] , and Maayane T. Soumagnac[16,17]
[1] Kavli Institute for Theoretical Physics, University of California, Santa Barbara, CA 93106, USA; tkupfer@ucsb.edu
[2] Division of Physics, Mathematics and Astronomy, California Institute of Technology, Pasadena, CA 91125, USA
[3] DIRAC Institute, Department of Astronomy, University of Washington, 3910 15th Avenue NE, Seattle, WA 98195, USA
[4] Department of Astronomy, Boston University, 725 Commonwealth Avenue, Boston, MA 02215, USA
[5] Department of Physics, University of Warwick, Coventry CV4 7AL, UK
[6] Department of Physics, University of California, Santa Barbara, CA 93106, USA
[7] Theoretical Astrophysics, 350-17, California Institute of Technology, Pasadena CA 91125, USA
[8] University of Washington, Department of Astronomy, Box 351580, Seattle, WA 98195, USA
[9] Dr. Karl Remeis-Observatory & ECAP, Astronomical Institute, Friedrich-Alexander University Erlangen-Nuremberg (FAU), Sternwartstr. 7, D-96049 Bamberg,
Germany
[10] Department of Physics & Astronomy, University of Sheffield, Sheffield S3 7RH, UK
[11] Instituto de Astrofísica de Canarias, Via Lactea s/n, La Laguna, E-38205 Tenerife, Spain
[12] Gabriel Murawski Private Observatory (SOTES), Poland
[13] Caltech Optical Observatories, California Institute of Technology, Pasadena, CA 91125, USA
[14] IPAC, California Institute of Technology, 1200 E. California Boulevard, Pasadena, CA 91125, USA
[15] Center for Data Driven Discovery, California Institute of Technology, Pasadena, CA 91125, USA
[16] Lawrence Berkeley National Laboratory, 1 Cyclotron Road, Berkeley, CA 94720, USA
[17] Department of Particle Physics and Astrophysics, Weizmann Institute of Science, Rehovot 76100, Israel

Abstract

We present the discovery of the second binary with a Roche lobe–filling hot subdwarf transferring mass to a white dwarf (WD) companion. This 56 minute binary was discovered using data from the Zwicky Transient Facility. Spectroscopic observations reveal an He-sdOB star with an effective temperature of $T_{\rm eff} = 33,700 \pm 1000$ K and a surface gravity of log $(g) = 5.54 \pm 0.11$. The GTC+HiPERCAM light curve is dominated by the ellipsoidal deformation of the He-sdOB star and shows an eclipse of the He-sdOB by an accretion disk as well as a weak eclipse of the WD. We infer a He-sdOB mass of $M_{\rm sdOB} = 0.41 \pm 0.04\,M_\odot$ and a WD mass of $M_{\rm WD} = 0.68 \pm 0.05\,M_\odot$. The weak eclipses imply a WD blackbody temperature of $63,000 \pm 10,000$ K and a radius $R_{\rm WD} = 0.0148 \pm 0.0020\,R_\odot$ as expected for a WD of such high temperature. The He-sdOB star is likely undergoing hydrogen shell burning and will continue transferring mass for $\approx$1 Myr at a rate of $10^{-9}\,M_\odot\,{\rm yr}^{-1}$, which is consistent with the high WD temperature. The hot subdwarf will then turn into a WD and the system will merge in $\approx$30 Myr. We suggest that Galactic reddening could bias discoveries toward preferentially finding Roche lobe–filling systems during the short-lived shell-burning phase. Studies using reddening-corrected samples should reveal a large population of helium core–burning hot subdwarfs with $T_{\rm eff} \approx 25,000$ K in binaries of 60–90 minutes with WDs. Though not yet in contact, these binaries would eventually come into contact through gravitational-wave emission and explode as a subluminous thermonuclear supernova or evolve into a massive single WD.

Unified Astronomy Thesaurus concepts: B subdwarf stars (129); Stellar evolution (1599); White dwarf stars (1799); Compact binary stars (283); Stellar accretion (1578)

1. Introduction

Subdwarf B stars (sdBs) are stars of spectral type B with luminosities below the main sequence. The formation mechanism and evolution of sdBs are still debated, although most sdBs are likely helium (He)–burning stars with masses $\approx 0.5\,M_\odot$ and thin hydrogen envelopes (Heber 1986, 2009, 2016). A large fraction are found in binary systems (Maxted et al. 2001; Napiwotzki et al. 2004) and the most compact ones have periods $\lesssim$1 hr (e.g., Vennes et al. 2012; Geier et al. 2013; Kupfer et al. 2017b, 2017a, 2020). Systems with orbital periods $\lesssim$2 h at the exit of the last common envelope will overflow their Roche lobe while the hot subdwarf is still burning helium (e.g., Savonije et al. 1986; Tutukov & Fedorova 1989; Tutukov & Yungelson 1990; Iben & Tutukov 1991; Yungelson 2008; Piersanti et al. 2014; Brooks et al. 2015).

So far only a few hot subdwarf binaries have been identified that will start mass transfer while the hot subdwarf is still burning helium in its core. The first discovered system is CD–30°11223, which has an orbital period of $P_{\rm orb} = 70.5$ minutes and will start mass transfer in $\approx$40 Myr (Vennes et al. 2012; Geier et al. 2013).

Most recently Kupfer et al. (2020) discovered ZTF J2130 +4420, the first system where the sdOB fills its Roche lobe and has started mass transfer to its white dwarf (WD) companion. In this Letter, we report the discovery of ZTF J205515.98+465106.5 (hereafter ZTF J2055+4651), the second confirmed member of Roche lobe–filling hot subdwarf stars in compact binaries. ZTF J2055+4651 was discovered in a period search using the conditional entropy period-finding algorithm (Graham et al. 2013) of all Pan-STARRS objects with colors of $g - r < 0.2$ and $r - i < 0.2$, and more than 50 ZTF measurements at the time, as

described in Burdge et al. ([2019](#)) and Coughlin et al. ([2020](#)). Conditional entropy is an information-theory-based algorithm that seeks to find the period that produces the most ordered (lowest entropy) arrangement of data points in the phase-folded light curve while also accounting for the phase space coverage of the data. Independently, on 2019 July 19, Gabriel Murawski reported the object to the International Variable Star Index (VSX).[18] Also, Sandoval et al. ([2020](#)) report the absence of X-ray emission from 3.7 ks Swift observations and found a limit for the X-ray flux of $<1 \times 10^{-13}$ erg s^{-1} cm^{-2} leading to a limit of $<6 \times 10^{31}$ erg s^{-1} at a distance of 2170 pc (Bailer-Jones et al. [2018](#)). We present the system properties, compare them to ZTF J2130+4420, and discuss possible implications for this new class of Roche lobe–filling hot subdwarf binaries.

2. Observations

As part of the Zwicky Transient Facility (ZTF), the Palomar 48-inch (P48) telescope images the sky every clear night. ZTF J2055+4651 was discovered as part of a dedicated high-cadence ZTF survey at low Galactic latitudes (Bellm et al. [2019a](#); Graham et al. [2019](#)), which either observed one field or alternated between two adjacent fields continuously for ≈1.5–3 hours on two to three consecutive nights in the ZTF-r band (Bellm et al. [2019b](#)). The high-cadence data were complemented by data from the ZTF public survey that was made available after data release 2 on 2019 December 11. Image processing of ZTF data is described in full detail in Masci et al. ([2019](#)). The ZTF light curve of ZTF J2055+4651 consists of 224 observations in ZTF-g and 496 observations in ZTF-r.

Additionally on 2019 September 5, ZTF J2055+4651 was observed with the Gran Telescopio Canarias (GTC) using HiPERCAM, which is a five-beam imager equipped with frame-transfer CCDs allowing the simultaneous acquisition of u_s, g_s, r_s, i_s, and z_s[19] band images at a rate of up to 1000 frames per second (Dhillon et al. [2016](#), [2018](#)). ZTF J2055+4651 was observed at a 3 s cadence with a dead time of 10 ms for 1130 frames with HiPERCAM. The run lasted 1 hr, covering a little more than one 56 minute binary orbit. The cadence in u_s and z_s alone was a factor of 3 slower than the other bands to optimize signal to noise. The data were reduced using the dedicated HiPERCAM pipeline,[20] including debiasing and flat-fielding. Differential photometry was also performed. Due to technical problems the i_s-band light curve could not be used for the analysis.

On 2019 July 30 a sequence of five optical spectra was obtained with the Shane telescope and the KAST spectrograph at Lick observatory using a low-resolution mode ($R \approx 1200$). The spectra were taken consecutively and had an exposure time of 12 minutes. Data reduction was performed with the standard IRAF packages. Although 12 minutes covers 1/5 of the orbit we detected large radial velocity shifts between the spectra, confirming the binary nature.

Additionally, on 2019 September 24 and 2019 September 25 phase-resolved spectroscopy of ZTF J2055+4651 was obtained using the Gemini-North Telescope, using Gemini Multi-Object Spectrograph (GMOS) in long-slit mode with the B600 grating

($R \approx 1400$). We obtained a total of 64 spectra with an exposure time of 3 minutes per spectrum. CuAr arc exposures were taken at the position of the target before and after each observing sequence to account for telescope flexure. The data were reduced using the IRAF package for GMOS.

3. Period Finding and Spectroscopic Analysis

As we followed the same procedure as described in Kupfer et al. ([2020](#)), we only briefly describe the major steps here. To derive the orbital period of the system, we use the ZTF light curve with its multi-month baseline in combination with the HiPERCAM light curve. The Gatspy (Vanderplas [2015](#); VanderPlas & Ivezić [2015](#)) module that utilizes the Lomb–Scargle periodogram (Lomb [1976](#); Scargle [1982](#)) was used for period finding, yielding $P_{\rm orb} = 56.34785(26)$ minutes. Using the parameter from the best light-curve fit (see Section [4](#)) and only fitting the zero-point of the ephemeris (T_o) to the HiPERCAM light curves, we find an ephemeris of

$$T_o({\rm BMJD}) = 58731.9639(90) + 0.03913045(18)E, \quad (1)$$

where E corresponds to the epoch.

We find spectral features of hydrogen and neutral (He I) and ionized (He II) helium lines typical for sdOB stars. By fitting the rest-wavelength corrected average Gemini spectrum with metal-free NLTE model spectra (Stroeer et al. [2007](#)), we determine $T_{\rm eff} = 33,700 \pm 1000$ K, $\log(g) = 5.54 \pm 0.11$, $\log y = \log[n({\rm He})/n({\rm H})] = 0.06 \pm 0.05$, and $v_{\rm rot} \sin i = 201 \pm 30$ km s^{-1}. Additionally, we measured atmospheric parameters using NLTE models computed with TLUSTY (Hubeny & Lanz [1995](#)) that include typical hot subdwarf abundances of nitrogen, carbon, and oxygen (Naslim et al. [2013](#)). We find fully consistent results with our metal-free NLTE models. Figure [1](#) shows the fit to the Gemini spectrum. The occurrence of both He I and He II as well as the increased helium abundance $\log y > 0$ classifies the hot subdwarf as an He-sdOB star (see Heber [2016](#)).

We folded the individual Gemini spectra on the ephemeris shown in Equation ([1](#)) into 20 phase-bins and coadded individual spectra observed at the same binary phase. This leads to a signal to noise per phase-bin of ≈30. We used the FITSB2 routine (Napiwotzki et al. [2004](#); Geier et al. [2011](#)) to then measure radial velocities. Assuming circular orbits, a sine curve was fitted to the folded radial velocity (RV) data points (Figure [2](#)) excluding the data points around Phase 0.8–0.2. We find a velocity semi-amplitude $K = 404.0 \pm 11.0$ km s^{-1}. Similar to ZTF J2130, the velocity deviates significantly from a pure sine curve around the phase when the sdOB is farthest away from the observer, which can be explained with the Rossiter–McLaughlin effect. The red curve in Figure [2](#) show the residuals predicted from the Rossiter–McLaughlin effect calculated from our best-fitting light-curve model.

4. Light-curve Analysis and System Parameter

The LCURVE code was used to perform the light-curve analysis of the HiPERCAM u_s, g_s, r_s, and z_s light curves (Copperwheat et al. [2010](#)). We assume a Roche lobe–filling sdOB star, a hot WD, and an irradiated disk around the WD. The passband specific beaming parameter B ($F_\lambda = F_{0,\lambda}[1 - B\frac{v_r}{c}]$; see Bloemen et al. [2011](#)) was calculated following the approximation from Loeb & Gaudi ([2003](#)). We use $B = 1.7$, 1.5, 1.37, and 1.25 for u_s, g_s, r_s, and z_s, respectively. The passband specific gravity-darkening (β) and limb-darkening (a_1, a_2, a_3, a_4) were fixed to the theoretical

---

[18] https://www.aavso.org/vsx/index.php?view=detail.top&oid=838260
[19] HiPERCAM uses high-throughput versions of the SDSS filters known as Super-SDSS filters, and we denote these filters u_s, g_s, r_s, etc.
[20] https://github.com/HiPERCAM/
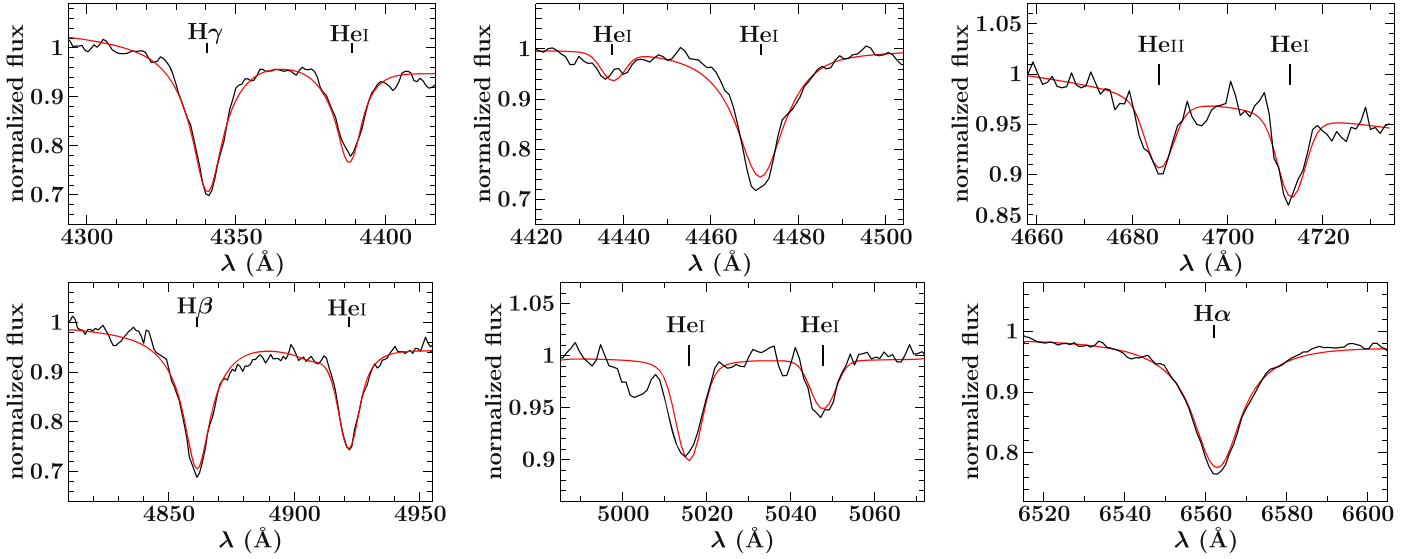
Figure 1. Fit of synthetic NLTE models to the hydrogen Balmer, as well as neutral and ionized helium lines of the coadded Gemini spectrum. The black solid line corresponds to the spectrum and red solid line to the fit.
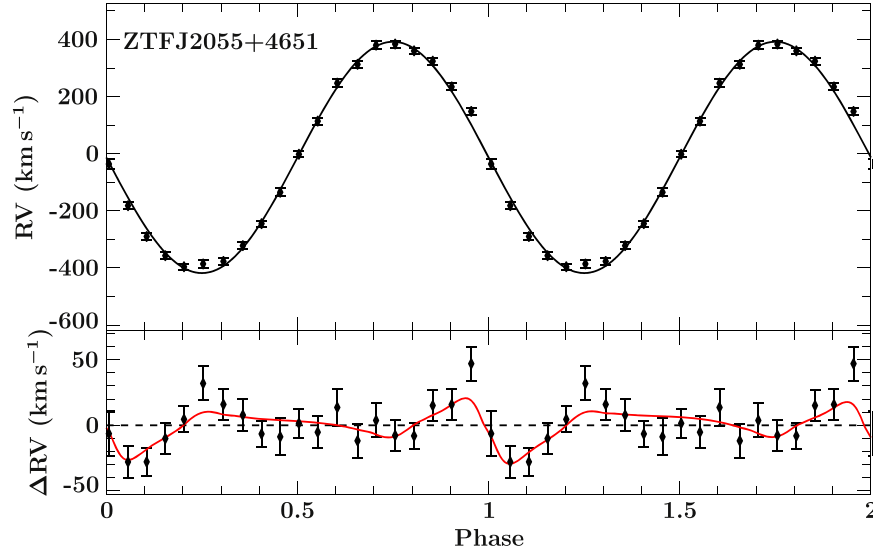

Figure 2. Measured radial velocity vs. orbital phase for ZTF J2055+4651. The RV data are phase folded with the orbital period and plotted twice for better visualization. The residuals are plotted below. The strong deviation from a pure sine curve around phase 0 (1) can be explained by the Rossiter–McLaughlin effect occurring when the accretion disk eclipses the rapidly rotating sdOB. The red curve shows the predicted residuals for the Rossiter–McLaughlin effect from our best-fitting model (see Section 4).

values from Claret & Bloemen (2011) for $T_{\rm eff} = 35,000$ K and $\log(g) = 5.00$ and solar metallicity. We used $\beta = 0.54$, $a_1 = 0.93$, $a_2 = -0.98$, $a_3 = 0.85$, and $a_4 = -0.29$ for u_s; $\beta = 0.42$, $a_1 = 0.96$, $a_2 = -1.05$, $a_3 = 0.87$, and $a_4 = -0.28$ for g_s; $\beta = 0.41$, $a_1 = 0.90$, $a_2 = -1.11$, $a_3 = 0.94$, and $a_4 = -0.31$ for r_s; and $\beta = 0.39$, $a_1 = 0.83$, $a_2 = -1.20$, $a_3 = 1.09$, and $a_4 = -0.38$ for z_s. We also tried to set the limb- and gravity-darkening parameters according to the tables of Claret et al. (2020) for hydrogen-rich atmospheres and found no significant difference in the final results. In addition, to account for any residual airmass effect we added a first-order polynomial. The best value of χ^2 for this model was around 3500 for 3012 points, which also includes a weak eclipse of the hot WD. Although the eclipse is weak ($\leqslant 1\%$), the χ^2 for the non-eclipsing solution is 3900, which is statistically significantly worse compared to the solution with the weak eclipse. For the final model we normalized the errors in the data to account for the small additional residuals

and obtain a reduced $\chi^2 \approx 1$. To determine the uncertainties in the parameters we combine LCURVE with emcee (Foreman-Mackey et al. 2013), an implementation of a Markov Chain Monte Carlo sampler that uses a number of parallel chains to explore the solution space. We use 256 chains and let them run until the chains stabilized to a solution, which took approximately 1500 generations. Figure 3 shows the best fit for each HiPER-CAM band.

Although ZTF J2055+4651 is a single-lined binary, we can still constrain the masses and radii of the two stars by combining the light-curve modeling with the spectroscopic fitting. Parameters derived in this way by a simultaneous fit to the HiPERCAM u_s, g_s, r_s, and z_s light curves are summarized in Table 1.

Our solution converges on a mass ratio of $q = M_1/M_2 = 0.60 \pm 0.03$, with individual masses of $M_{\rm He-sdOB} = 0.41 \pm 0.04$ $M_\odot$ and $M_{\rm WD} = 0.68 \pm 0.05$ $M_\odot$. The inclination is $i = 83.4 \pm 1°.0$ and the He-sdOB is Roche lobe–filling and has a
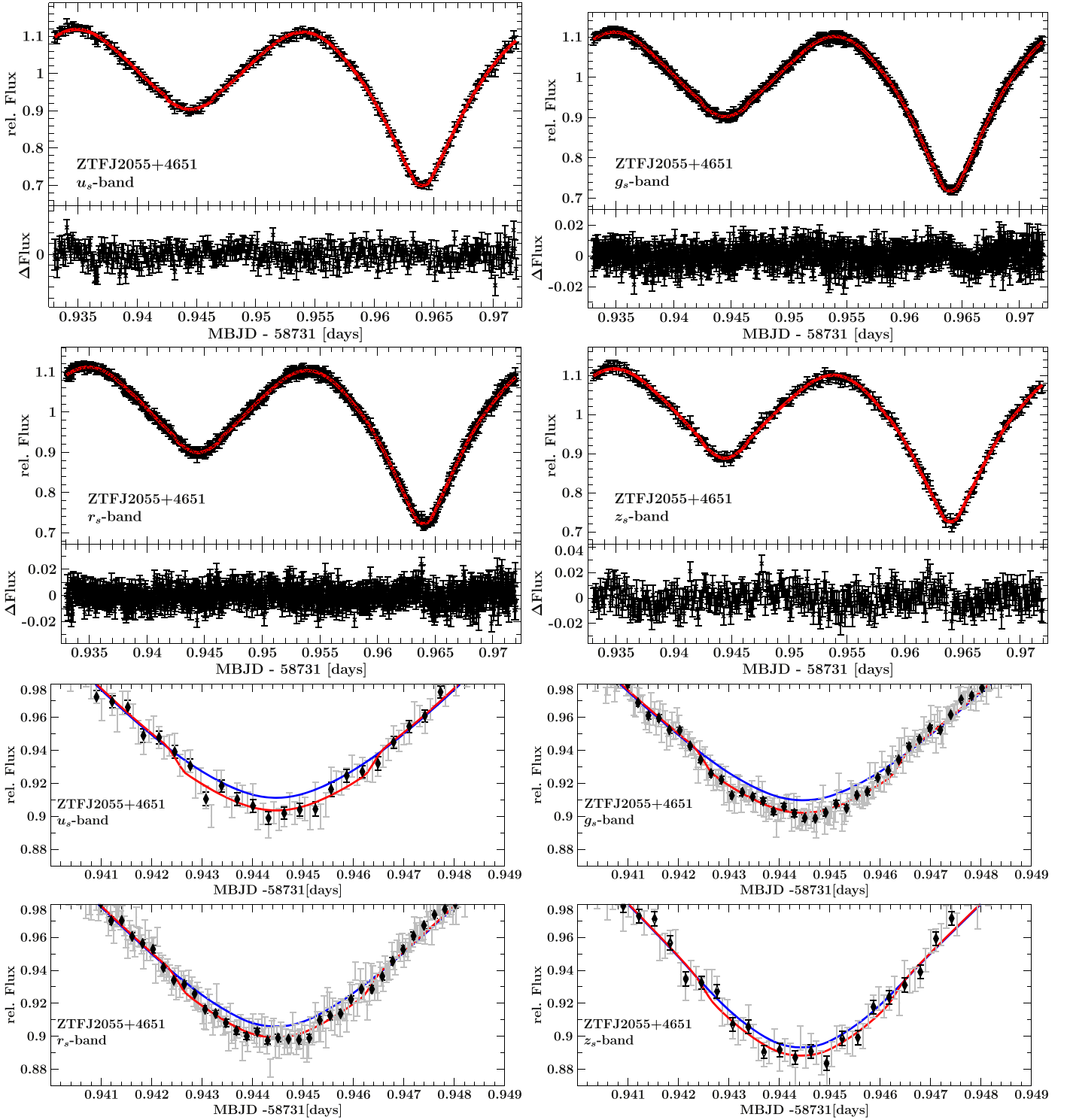
Figure 3. HiPERCAM light curves unbinned (gray) and binned (black) shown together with the LCURVE fit (red) observed optical Super-SDSS bandpasses. The deeper dip corresponds to an eclipse of the He-sdOB by the accretion disk, whereas the shallow dip originates in the ellipsoidal deformation of the sdOB star. The lower four panels show the region when the hot WD is being eclipsed by the He-sdOB. The blue solid curve marks the same model without eclipses of the hot WD.

volumetric-corrected radius of $R_{\rm sdOB} = 0.17 \pm 0.01 \, R_\odot$ (Table 1). We find that the He-sdOB would have a projected rotational velocity $v_{\rm rot} \sin i = 215 \pm 6 \, \rm km \, s^{-1}$ if synchronized to the orbit, consistent with the observed $v_{\rm rot} \sin i = 201 \pm 30 \, \rm km \, s^{-1}$. We detect a weak eclipse of the hot WD that constrains its properties (Figure 3). We derive a blackbody temperature of $63,000 \pm 10,000 \, \rm K$ for the WD, with a radius of $0.0148 \pm 0.0020 \, R_\odot$, which

is 10%–50% larger than a fully degenerate WD. This is consistent with predictions for hot WDs as shown in Romero et al. (2019), who predict 25% increased radius for a carbon–oxygen WD with $T_{\rm eff} = 60,000 \, \rm K$ and a hydrogen layer of $M = 10^{-4} \, M_\odot$.

The spectral energy distribution (SED) in combination with the Gaia parallax allows for an independent estimate of the stellar parameters of the hot subdwarf. To this end, we first

Table 1
Measured and Derived Parameters for ZTF J2055+4651

Right ascension[a]	R.A. (hr)	20:55:15.98
Declination[a]	decl. (°)	+46:51:06.46
Magnitude[b]	g (mag)	17.72 ± 0.04
Parallax[a]	ϖ (mas)	0.432 ± 0.098
Distance	d (kpc)	$2.3^{+0.7}_{-0.4}$
reddening[c]	$E(g-r)$ (mag)	0.46 ± 0.03
Absolute magnitude (reddening corrected)[d]	M_g (mag)	4.4 ± 0.6
Proper motion (R.A.)[a]	$\mu_\alpha \cos(\delta)$ (mas yr^{-1})	-3.33 ± 0.17
Proper motion (decl.)[a]	μ_δ (mas yr^{-1})	-5.160 ± 0.167
Atmospheric and Orbital Parameters of the sdOB from Spectroscopic Fits		
Effective temperature	$T_{\rm eff}$ (K)	$33,700 \pm 1000$
Surface gravity	$\log(g)$	5.54 ± 0.11
Helium abundance	$\log y$	0.06 ± 0.05
Projected rotational velocity	$v_{\rm rot} \sin i$ (km s^{-1})	201 ± 30
RV semi-amplitude (sdOB)	K (km s^{-1})	404.0 ± 11.0
System velocity	γ (km s^{-1})	-20.0 ± 6.0
Binary mass function	$f_{\rm m}$ ($M_\odot$)	0.267 ± 0.022
Derived Parameters from Light-curve Fit Combined with Spectroscopic Results		
Ephemeris zero-point	T_0 (MBJD)	58731.9639(90)
Orbital period	$P_{\rm orb}$ (min)	56.34785(26)
Mass ratio	$q = \frac{M_{\rm sdOB}}{M_{\rm WD}}$	0.60 ± 0.03
sdOB mass	$M_{\rm sdOB}$ ($M_\odot$)	0.41 ± 0.04
sdOB radius	$R_{\rm sdOB}$ ($R_\odot$)	0.17 ± 0.01
WD mass	$M_{\rm WD}$ ($M_\odot$)	0.68 ± 0.05
WD radius	$R_{\rm WD}$ ($M_\odot$)	0.0148 ± 0.0020
Orbital inclination	i (°)	83.4 ± 1.0
Separation	a ($R_\odot$)	0.50 ± 0.01
Derived Parameters from Spectrophotometry and Parallax[e]		
Color excess	$E(44-55)$	0.559 ± 0.021 mag
Angular diameter	$\log(\Theta \, ({\rm rad}))$	-11.479 ± 0.011
sdOB radius	$R = \Theta/(2\varpi)$ ($R_\odot$)	$0.17^{+0.05}_{-0.04}$
sdOB mass	$M = gR^2/G$ ($M_\odot$)	$0.37^{+0.29}_{-0.14}$
Luminosity	$L/L_\odot = (R/R_\odot)^2(T_{\rm eff}/\,T_{\rm eff,\odot})^4$	34^{+24}_{-12}

Notes.
[a] Taken from Gaia DR2, epoch 2015.5 (Gaia Collaboration et al. 2016, 2018).
[b] Taken from PanSTARRS DR1 (Chambers et al. 2016).
[c] Taken from 3D extinction maps (Green et al. 2019).
[d] Reddening corrected with 3D extinction maps from Green et al. (2019).
[e] The given uncertainties are single-parameter 1σ confidence intervals based on χ^2 statistics. A generic excess noise of 0.026 mag has been added in quadrature to all photometric measurements to achieve a reduced χ^2 of unity at the best fit.

construct the observed SED from Gaia (Evans et al. 2018) and PanSTARRS photometry (Chambers et al. 2016).[21] Using the atmospheric parameters derived by spectroscopy, a synthetic SED is computed with an updated version of ATLAS12 (Kurucz 1996; Irrgang et al. 2018), which is then matched to the observed SED by fitting the angular diameter Θ as a

distance scaling factor and $E(44-55)$ as an interstellar reddening parameter (see Heber et al. 2018 for details). The interstellar extinction law by Fitzpatrick et al. (2019) is used. The results are summarized in Table 1 and visualized in Figure 4. As expected for a star in the Galactic disk, reddening is large ($E(44-55) = 0.559 \pm 0.021$ mag).

In combination with the Gaia parallax ϖ and the atmospheric parameters ($T_{\rm eff}$ and $\log(g)$) the angular diameter allows us to determine the stellar parameters ($R_{\rm sdOB}$, $M_{\rm sdOB}$, and luminosity $L_{\rm sdOB}$). Results are listed Table 1. The mass derived for the hot subdwarf agrees well with that derived from the light curve, although the uncertainty of the former is large because of the $\approx25\%$ parallax error and 0.11 dex $\log(g)$ error.

Using 3D extinction maps provided by Green et al. (2019)[22] toward the direction of ZTF J2055+4651, we find a reddening of $E(g-r) = 0.46 \pm 0.03$ at a distance of $2.3^{+0.7}_{-0.4}$ kpc, which is somewhat lower than the reddening derived by the SED analysis. Nonetheless, ZTF J2055+4651 is highly reddened and has a PanSTARRS color of $g - r = 0.07$ mag (Chambers et al. 2016). Such a color puts it in the regime of A- to F-type stars with $T_{\rm eff} \approx 10,000$ K, which is significantly cooler than typical hot subdwarfs. With the 3D map extinction maps corrected magnitude, we find an absolute magnitude of $M_{\rm g} = 4.4 \pm 0.6$ mag, consistent with a hot subdwarf star (Geier et al. 2019).

To put constraints on the population origin of ZTF J2055+ 4651 we calculated its kinematics. The proper motions of the system is taken from the Gaia data release 2 catalog (Gaia Collaboration et al. 2018; $\mu_\alpha \cos(\delta) = -3.326 \pm 0.167$ mas yr^{-1}, $\mu_\delta = -5.160 \pm 0.167$ mas yr^{-1}). We followed the same approach as described in Kupfer et al. (2020) following Odenkirchen & Brosche (1992) and Pauli et al. (2006). We use the Galactic potential of Allen & Santillan (1991) as revised by Irrgang et al. (2013). The orbit was integrated from the present to 3 Gyr into the past. ZTF J2055+4651 moves between a distance of 8.6 to 11.6 kpc from the Galactic center with an eccentricity of 0.07 within a height of 50 pc of the Galactic equator. Exactly as for the other Roche lobe–filling hot subdwarf binary, ZTF J2130+ 4420, ZTF J2055+4651 is a member of the Galactic thin-disk population.

5. Discussion

5.1. Evolution

Following the same prescription as described in full detail in Section 6.2 in Kupfer et al. (2020) we employed MESA version 12115 (Paxton et al. 2011, 2013, 2015, 2018, 2019) to construct evolutionary models for ZTF J2055+4651. To match the observed properties of ZTF J2055+4651, we start with a MESA model of a progenitor star with a mass of $2.9\,M_\odot$, which has a main-sequence lifetime of 350 Myr. Once the main-sequence star starts to evolve onto the red giant branch (RGB) He core burning starts under nondegenerate conditions. We remove most of the hydrogen-rich envelope, leaving a He core–burning sdB with $T_{\rm eff} \approx 25,000$ K, a core mass of $0.36\,M_\odot$, and a thin H/He envelope of $0.03\,M_\odot$. The envelope is defined by where the H mass fraction is above $0.01\,M_\odot$. This subdwarf model is then placed in a binary with a $0.65\,M_\odot$ WD with an orbital period of ≈140 min. Gravitational-wave radiation removes angular momentum from the binary and shortens the

---

[21] Based on averages of 223 epochs of good Gaia observations and of 80 epochs of PanSTARRS observations.

[22] http://argonaut.skymaps.info/
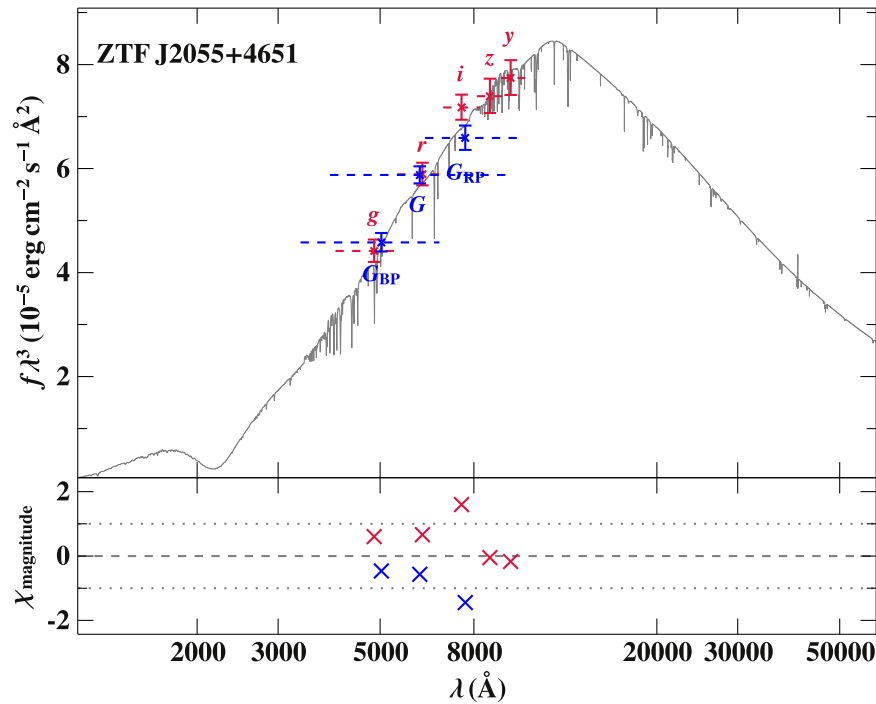
Figure 4. Comparison of synthetic and observed photometry: The top panel shows the SED. The colored data points are filter-averaged fluxes that were converted from observed magnitudes (the respective filter widths are indicated by the dashed horizontal lines), while the gray solid line represents the best-fitting model, i.e., it is based on the parameters from Table 1, degraded to a spectral resolution of 6 Å. The flux is multiplied with the wavelength to the power of three to reduce the steep slope of the SED. The bottom panel shows the residual χ, i.e., the difference between synthetic and observed magnitudes divided by the corresponding uncertainties. Only the angular diameter Θ and the color excess $E(B - V)$ are free fitting parameters. Pan-STARRS1 magnitudes (Chambers et al. (2016)) are shown in red and Gaia magnitudes (Evans et al. 2018) with corrections and calibrations from Maíz Apellániz & Weiler (2018) in blue.

period. The period does not shrink far enough during He core burning, which lasts ≈ 350 Myr, that the sdB fills its Roche lobe (see the left panel in Figure 5).

Once He core burning finishes the core contracts and hydrogen burning starts, the radius of the hot subdwarf expands beyond its Roche radius, and mass transfer starts at an orbital period close to the observed orbital period. Mass transfer will continue for ≈ 1 Myr at a rate exceeding $10^{-9} M_{\odot}$ yr^{-1} until hydrogen shell burning is finished and the star contracts to become a carbon–oxygen WD with a thick helium layer and a small residual layer of hydrogen. The high accretion rate will heat the accreting WD significantly (Townsley & Bildsten 2003). Models predict a $T_{\rm eff} \approx 50,000$ K for accretion rates of $10^{-9} M_{\odot}$ yr^{-1} (Burdge et al. 2019) consistent with the high blackbody temperature of the accretor observed in ZTF J2055+4651. Accretion onto the WD companion at this rate will cause unstable hydrogen ignition after $\approx 10^{-4} M_{\odot}$ accumulates, leading to classical novae eruptions (Nomoto 1982; Nomoto et al. 2007; Wolf et al. 2013). This accretion rate predicts a recurrence time of order 10^5 yr for a total of approximately 10 novae. Our binary model suggests that this system is within the first $\approx 10\%$ of the 1 Myr accretion phase. At the current state the orbit will shrink with $\dot{P} \approx -6 \times 10^{-13}$ s s^{-1}, which will be detectable after a few years of monitoring. The right panel of Figure 5 shows the evolution of the donor through this mass transfer phase. After accretion has ceased, the orbit of the system will continue to shrink due to the radiation of gravitational waves and the system will merge in ≈ 30 Myr. Our models predict that there is a substantial He layer of $\approx 0.05 M_{\odot}$ left in the former hot subdwarf and the total mass of the system is relatively high ($M_{\rm total} \approx 1.1 M_{\odot}$). Recent models predict that such a system explodes as a subluminous thermonuclear supernova (Perets et al. 2019; Zenati et al. 2019). If the system avoids a thermonuclear

supernova it will merge and could evolve into a rapidly rotating single high-mass carbon–oxygen WD (Saio 2008; Clayton 2012; Schwab 2019).

5.2. The Accretion Disk

Our Gemini spectra show no evidence for any disk lines, which limits the accretion disk contribution of the accretion disk to the overall luminosity to $\leqslant 5\%$. Our models predict an accretion rate of $10^{-9} M_{\odot}$ yr^{-1}. From that we can limit the accretion luminosity to be ≈ 1.5 L$_{\odot}$ which is significantly smaller than the luminosity of the sdOB star and in agreement with the absence of any signs of the disk in the optical spectra.

Sandoval et al. (2020) reported the nondetection of X-rays in a 3.6 ks observation with the Neil Gehrels Swift Observatory. X-rays from disk-accreting WDs are generally emitted from the boundary layer. We expect that $\approx 50\%$ of the accretion luminosity is released in the boundary layer. This corresponds to $\approx 3 \times 10^{31}$ erg s^{-1}, which is $\approx 50\times$ larger than the X-ray upper limit. This suggests an optically thick boundary layer in ZTF J2055+4651 with most flux emitted in the extreme UV. This has been observed in SS Cyg, where the X-ray luminosity dropped and the extreme UV emission increased during outburst, as the accretion rate increased (Wheatley et al. 2003).

5.3. Implications for a Population of Roche Lobe–filling Hot Subdwarfs

Kupfer et al. (2020) presented the first known Roche lobe–filling hot subdwarf binary. ZTF J2055+4651 is the second known system and the overall evolution appears to be similar to ZTF J2130+4420. Both systems have $M_{\rm sdOB} < 0.47 M_{\odot}$ hot subdwarf masses and likely evolved from stars with masses
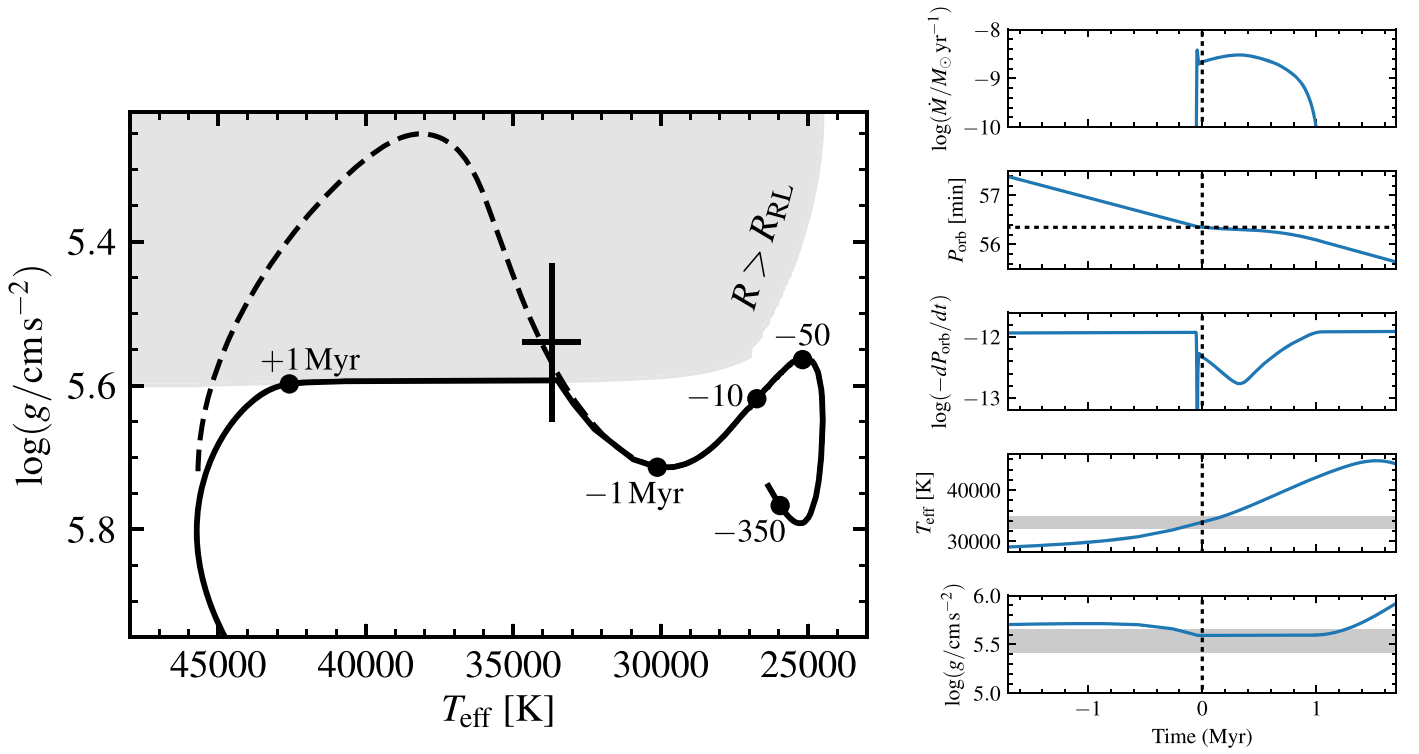
Figure 5. Left: evolution track for the 0.39 $M_\odot$ hot subdwarf model. The gray shaded region shows the maximum radius R that the subdwarf can reach before overflowing its Roche lobe radius R_{RL}, which shrinks over time due to gravitational-wave radiation. The black dashed curve shows the evolution track for a single-star evolution model of the hot subdwarf that is not confined by the Roche lobe. The black points label ages (in Myr) along the track relative to the present time. Right: time evolution of the MESA binary model through the mass transfer phase leading up to the currently observed state defined by $P_{orb} = 56.35$ minutes at time 0. Gray shaded regions in the lower two panels show the measured values of T_{eff} and $\log(g)$ given in Table 1.

$>2\,M_\odot$ and therefore are members of a young stellar population consistent with the observed Galactic kinematics. This result is also consistent with predictions by Han et al. (2003), who found that the most compact hot subdwarf binaries with a compact companion are expected to evolve from main-sequence stars with masses $>2\,M_\odot$. Their study showed that hot subdwarf binaries formed with orbital periods $\lesssim 2$ hr are dominated by systems with progenitor masses $>2\,M_\odot$.

ZTF J2130+4420 and ZTF J2055+4651 are hotter compared to most known hot subdwarfs and can be best explained as donor stars during the shell-burning phase. Given that the residual hydrogen shell-burning lifetime of the hot subdwarf is a factor of ≈ 10–100 shorter than its helium core-burning lifetime we expect a population ≈ 10–100 larger of systems during core burning. We suggest here that Galactic reddening could bias discoveries toward preferentially finding Roche lobe–filling systems during shell burning.

Systems located at low Galactic latitudes will suffer from extinction and reddening. Although the exact extinction is direction dependent, on average the Galactic plane has an extinction of ≈ 1 mag per kpc in the optical bands where bluer bands are more strongly affected (Gontcharov 2016; Green et al. 2019). This leads to a shift of PanSTARRS $g - r$ colors of ≈ 0.25–0.3 mag per kpc toward redder color leading to a biased sample of hotter or less distant systems in color-selected samples. Typically hot subdwarfs have PanSTARRS colors of $g - r \approx -0.35$ mag (Geier et al. 2019) leading to $g - r \approx 0.15$–0.25 mag for a 2 mag extinction at a distance of 2 kpc. These are typical colors for F- to G-type main-sequence stars and such objects will be missed in color-selected samples for blue stars. Only a reddening-corrected sample, which requires distance estimates,

will allow candidates to be selected in regions with significant extinction. However, particularly in dense Galactic plane regions, Gaia DR2 data often provide bad astrometry, resulting in many spurious sources. Therefore, hot subdwarfs selected based on absolute magnitudes with reddening corrections are currently done best outside the Galactic plane with no crowding (Geier et al. 2019), but misses these hot subdwarfs at low Galactic latitudes that have evolved from a young stellar population and progenitor masses $>2\,M_\odot$.

Further discoveries and extended studies using reddening-corrected samples are needed for space density calculations and to understand whether Roche lobe–filling hot subdwarfs are more common among shell-burning hot subdwarfs rather than He core–burning hot subdwarf stars.

6. Conclusions and Summary

ZTF J2055+4651 was discovered as a $P_{orb} = 56.34785(26)$ minute variable with a light-curve shape similar to ZTF J2130+4420. Follow-up observations show that ZTF J2055+4651 is the second Roche lobe–filling hot subdwarf binary known today. High signal-to-noise ratio photometry obtained with HiPERCAM in combination with Gemini spectroscopy constrain the system parameters to a mass ratio $q = M_{sdOB}/M_{WD} = 0.60 \pm 0.03$, a mass for the sdOB $M_{sdOB} = 0.41 \pm 0.04\,M_\odot$, and a WD companion mass $M_{WD} = 0.68 \pm 0.05\,M_\odot$. Additionally, the HiPERCAM light curve revealed a weak ($\approx 1\%$) eclipse of the hot WD that allowed us to constrain its blackbody temperature to $63,000 \pm 10,000$ K.

We use the stellar evolution code MESA to compute the evolution of the system and find that the hot subdwarf formed

in a common envelope phase at a period of $\approx$140 minutes and filled its Roche lobe close to the observed period when the hot subdwarf expanded during residual hydrogen shell burning. We predict that the binary will transfer mass for $\approx$1 Myr and we currently observe the binary in its first 10% of this phase. Our models predict a mass transfer rate of more than $10^{-9}\,M_\odot\,\mathrm{yr}^{-1}$. Due to its high total mass the system will merge in $\approx$30 Myr and either explode as subluminous type Ia supernova (Perets et al. 2019; Zenati et al. 2019) or merge and form a massive single WD (Webbink 1984; Saio 2008; Clayton 2012; Schwab 2019).

ZTF J2055+4651 and ZTF J2130+4420 are the only known binaries with a Roche lobe–filling hot subdwarf donor. Both systems have similar properties and we see mass transfer during the short-lived hydrogen shell–burning phase compared to the He core–burning phase, which lasts significantly longer. The most likely explanation is a selection criteria bias against more typical hot subdwarfs with $T_{\rm eff} \approx 25{,}000$ K due to severe reddening at low Galactic latitudes. Future studies require reddening-corrected samples. We predict that a substantial population of He core–burning Roche lobe–filling hot subdwarf binaries can still be discovered at low Galactic latitudes in young stellar populations.

ORCID iDs

Thomas Kupfer ⓘ https://orcid.org/0000-0002-6540-1484
Evan B. Bauer ⓘ https://orcid.org/0000-0002-4791-6724
Kevin B. Burdge ⓘ https://orcid.org/0000-0002-7226-836X
Jan van Roestel ⓘ https://orcid.org/0000-0002-2626-2872
Eric C. Bellm ⓘ https://orcid.org/0000-0001-8018-5348
Jim Fuller ⓘ https://orcid.org/0000-0002-4544-0750
JJ Hermes ⓘ https://orcid.org/0000-0001-5941-2286
Thomas R. Marsh ⓘ https://orcid.org/0000-0002-2498-7589
Shrinivas R. Kulkarni ⓘ https://orcid.org/0000-0001-5390-8563
E. S. Phinney ⓘ https://orcid.org/0000-0002-9656-4032
Thomas A. Prince ⓘ https://orcid.org/0000-0002-8850-3627
Paula Szkody ⓘ https://orcid.org/0000-0003-4373-7777
Yuhan Yao ⓘ https://orcid.org/0000-0001-6747-8509
Andreas Irrgang ⓘ https://orcid.org/0000-0002-0465-3725
Ulrich Heber ⓘ https://orcid.org/0000-0001-7798-6769
Vik S. Dhillon ⓘ https://orcid.org/0000-0003-4236-9642
Gabriel Murawski ⓘ https://orcid.org/0000-0001-7809-1457
Dmitry A. Duev ⓘ https://orcid.org/0000-0001-5060-8733
Matthew J. Graham ⓘ https://orcid.org/0000-0002-3168-0139
Russ R. Laher ⓘ https://orcid.org/0000-0003-2451-5482
S. P. Littlefair ⓘ https://orcid.org/0000-0001-7221-855X
A. A. Mahabal ⓘ https://orcid.org/0000-0003-2242-0244
Frank J. Masci ⓘ https://orcid.org/0000-0002-8532-9395
Ben Rusholme ⓘ https://orcid.org/0000-0001-7648-4142

David L. Shupe https://orcid.org/0000-0003-4401-0430
Maayane T. Soumagnac https://orcid.org/0000-0001-6753-1488

References

Allen, C., & Santillan, A. 1991, RMxAA, 22, 255
Astropy Collaboration, Price-Whelan, A. M., Sipőcz, B. M., et al. 2018, AJ, 156, 123
Astropy Collaboration, Robitaille, T. P., Tollerud, E. J., et al. 2013, A&A, 558, A33
Bailer-Jones, C. A. L., Rybizki, J., Fouesneau, M., Mantelet, G., & Andrae, R. 2018, AJ, 156, 58
Bellm, E. C., Kulkarni, S. R., Barlow, T., et al. 2019b, PASP, 131, 068003
Bellm, E. C., Kulkarni, S. R., Graham, M. J., et al. 2019a, PASP, 131, 018002
Bloemen, S., Marsh, T. R., Østensen, R. H., et al. 2011, MNRAS, 410, 1787
Brooks, J., Bildsten, L., Marchant, P., & Paxton, B. 2015, ApJ, 807, 74
Burdge, K. B., Coughlin, M. W., Fuller, J., et al. 2019, Natur, 571, 528
Chambers, K. C., Magnier, E. A., Metcalfe, N., et al. 2016, arXiv:1612.05560
Claret, A., & Bloemen, S. 2011, A&A, 529, A75
Claret, A., Cukanovaite, E., Burdge, K., et al. 2020, A&A, 634, A93
Clayton, G. C. 2012, JAVSO, 40, 539
Copperwheat, C. M., Marsh, T. R., Dhillon, V. S., et al. 2010, MNRAS, 402, 1824
Coughlin, M. W., Burdge, K., Phinney, E. S., et al. 2020, MNRAS, 494, L91
Dhillon, V., Dixon, S., Gamble, T., et al. 2018, Proc. SPIE, 10702, 107020L
Dhillon, V. S., Marsh, T. R., Bezawada, N., et al. 2016, Proc. SPIE, 9908, 99080Y
Evans, D. W., Riello, M., De Angeli, F., et al. 2018, A&A, 616, A4
Fitzpatrick, E. L., Massa, D., Gordon, K. D., Bohlin, R., & Clayton, G. C. 2019, ApJ, 886, 108
Foreman-Mackey, D., Hogg, D. W., Lang, D., & Goodman, J. 2013, PASP, 125, 306
Gaia Collaboration, Brown, A. G. A., Vallenari, A., et al. 2018, A&A, 616, A1
Gaia Collaboration, Prusti, T., de Bruijne, J. H. J., et al. 2016, A&A, 595, A1
Geier, S., Hirsch, H., Tillich, A., et al. 2011, A&A, 530, A28
Geier, S., Marsh, T. R., Wang, B., et al. 2013, A&A, 554, A54
Geier, S., Raddi, R., Gentile Fusillo, N. P., & Marsh, T. R. 2019, A&A, 621, A38
Gontcharov, G. A. 2016, Ap, 59, 548
Graham, M. J., Drake, A. J., Djorgovski, S. G., Mahabal, A. A., & Donalek, C. 2013, MNRAS, 434, 2629
Graham, M. J., Kulkarni, S. R., Bellm, E. C., et al. 2019, PASP, 131, 078001
Green, G. M., Schlafly, E. F., Zucker, C., Speagle, J. S., & Finkbeiner, D. P. 2019, arXiv:1905.02734
Han, Z., Podsiadlowski, P., Maxted, P. F. L., & Marsh, T. R. 2003, MNRAS, 341, 669
Heber, U. 1986, A&A, 155, 33
Heber, U. 2009, ARA&A, 47, 211
Heber, U. 2016, PASP, 128, 082001
Heber, U., Irrgang, A., & Schaffenroth, J. 2018, OAst, 27, 35
Houck, J. C., & Denicola, L. A. 2000, in ASP Conf. Ser. 216, Astronomical Data Analysis Software and Systems IX, ed. N. Manset, C. Veillet, & D. Crabtree (San Francisco, CA: ASP), 591
Hubeny, I., & Lanz, T. 1995, ApJ, 439, 875
Hunter, J. D. 2007, CSE, 9, 90
Iben, I., Jr., & Tutukov, A. V. 1991, ApJ, 370, 615
Irrgang, A., Kreuzer, S., Heber, U., & Brown, W. 2018, A&A, 615, L5
Irrgang, A., Wilcox, B., Tucker, E., & Schiefelbein, L. 2013, A&A, 549, A137
Kupfer, T., Bauer, E. B., Marsh, T. R., et al. 2020, ApJ, 891, 45
Kupfer, T., Ramsay, G., van Roestel, J., et al. 2017a, ApJ, 851, 28
Kupfer, T., van Roestel, J., Brooks, J., et al. 2017b, ApJ, 835, 131
Kurucz, R. L. 1996, in ASP Conf. Ser. 108, M.A.S.S., Model Atmospheres and Spectrum Synthesis, ed. S. J. Adelman, F. Kupka, & W. W. Weiss (San Francisco, CA: ASP), 160
Loeb, A., & Gaudi, B. S. 2003, ApJL, 588, L117
Lomb, N. R. 1976, Ap&SS, 39, 447
Maíz Apellániz, J., & Weiler, M. 2018, A&A, 619, A180
Masci, F. J., Laher, R. R., Rusholme, B., et al. 2019, PASP, 131, 018003
Maxted, P. f. L., Heber, U., Marsh, T. R., & North, R. C. 2001, MNRAS, 326, 1391
Napiwotzki, R., Karl, C. A., Lisker, T., et al. 2004, Ap&SS, 291, 321
Naslim, N., Jeffery, C. S., Hibbert, A., & Behara, N. T. 2013, MNRAS, 434, 1920
Nomoto, K. 1982, ApJ, 253, 798
Nomoto, K., Saio, H., Kato, M., & Hachisu, I. 2007, ApJ, 663, 1269
Odenkirchen, M., & Brosche, P. 1992, AN, 313, 69
Oliphant, T. E. 2015, Guide to NumPy (2nd ed.; USA: CreateSpace)
Pauli, E.-M., Napiwotzki, R., Heber, U., Altmann, M., & Odenkirchen, M. 2006, A&A, 447, 173
Paxton, B., Bildsten, L., Dotter, A., et al. 2011, ApJS, 192, 3
Paxton, B., Cantiello, M., Arras, P., et al. 2013, ApJS, 208, 4
Paxton, B., Marchant, P., Schwab, J., et al. 2015, ApJS, 220, 15
Paxton, B., Schwab, J., Bauer, E. B., et al. 2018, ApJS, 234, 34
Paxton, B., Smolec, R., Schwab, J., et al. 2019, ApJS, 243, 10
Perets, H. B., Zenati, Y., Toonen, S., & Bobrick, A. 2019, arXiv:1910.07532
Perley, D. A. 2019, PASP, 131, 084503
Piersanti, L., Tornambé, A., & Yungelson, L. R. 2014, MNRAS, 445, 3239
Romero, A. D., Kepler, S. O., Joyce, S. R. G., Lauffer, G. R., & Córsico, A. H. 2019, MNRAS, 484, 2711
Saio, H. 2008, in ASP Conf. Ser. 391, Hydrogen-Deficient Stars, ed. A. Werner & T. Rauch (San Francisco, CA: ASP), 69
Sandoval, L. R., Murawski, G., Copperwheat, C., & Maccarone, T. 2020, ATel, 13444, 1
Savonije, G. J., de Kool, M., & van den Heuvel, E. P. J. 1986, A&A, 155, 51
Scargle, J. D. 1982, ApJ, 263, 835
Schwab, J. 2019, ApJ, 885, 27
Stroeer, A., Heber, U., Lisker, T., et al. 2007, A&A, 462, 269
Townsley, D. M., & Bildsten, L. 2003, ApJL, 596, L227
Tutukov, A. V., & Fedorova, A. V. 1989, SvA, 33, 606
Tutukov, A. V., & Yungelson, L. R. 1990, SvA, 34, 57
Vanderplas, J. 2015, gatspy: General tools for Astronomical Time Series in Python, v0.3.0, Zenodo, doi:10.5281/zenodo.14833
VanderPlas, J. T., & Ivezić, v. 2015, ApJ, 812, 18
Vennes, S., Kawka, A., O'Toole, S. J., Németh, P., & Burton, D. 2012, ApJL, 759, L25
Webbink, R. F. 1984, ApJ, 277, 355
Wheatley, P. J., Mauche, C. W., & Mattei, J. A. 2003, MNRAS, 345, 49
Wolf, W. M., Bildsten, L., Brooks, J., & Paxton, B. 2013, ApJ, 777, 136
Yungelson, L. R. 2008, AstL, 34, 620
Zenati, Y., Toonen, S., & Perets, H. B. 2019, MNRAS, 482, 1135